Unexpected Effects of Surfactant Adsorption Upon Water/Vapor Surface Geometry and Fluctuations

Nitesh Kumar[a*] and Aurora E Clark[a,b*]
[a] *Department of Chemistry, University of Utah, Salt Lake City, UT, 84112*
[b] *Pacific Northwest National Laboratory, Richland, Washington 99354, United States.*
[*] *E-mail: nitesh.kumar@utah.edu, aurora.clark@utah.edu*
(Dated: November 25, 2023)

Exploring the effects of adsorbed surfactants surface geometry has is fundamental to various disciplines ranging from separations to catalysis. This study examines the influence of surfactant adsorption on surface geometric descriptors relevant to capillary wave fluctuations at the water/air interface using a coarse-grained instantaneous representation of the surface. Unexpected relationships are observed relative to that found in liquid/liquid interfaces of pure solvents and the pure water/vapor surface. In the case of concentration dependent tributyl phosphate adsorption, the surface develops sharper and less broad waves with increased TBP until a critical concentration in agreement with TBP self-assembly is reached. Thereafter the convexity and concavity of the surface stop cancelling each other. As the alkyl groups on the phopsphate head group are shortened (to form triethyl, tripropyl and trimethyl phosphate), the surface activity necessarily decreases. Yet the ability of the surfactant to increase surface fluctuations is dramatically increased.

Keywords: Molecular Adsorption, Capillary Wave Fluctuations, Surface Curvature, Instantaneous Surface.

Liquid/liquid and liquid/vapor interfaces catalyze numerous biological and chemical reactions.[1, 2] Their temporal dynamics, including but not limited to capillary waves[3–5] create unique topographical features (crests and troughs)[4] with different chemical properties.[6] Surfactant adsorption can either enhance or diminish surface fluctuations[7, 8] and impact properties such as interfacial tension and width.[7, 9, 10] These properties are further influenced by factors such as surfactant concentration, head-group polarity, or hydrophobic chain length.[11, 12]

Within capillary wave theory the Hamiltonian (H) for the system is the work done to change the surface area from ideal plane to the capillary wave surface. Different formulations for H can be written in terms of surface waves or interfacial characteristics. We use the simplest definition of the free energy of deformation (ΔG_{def}) as the expectation value of H being the change in the surface area (ΔA) multiplied by the surface tension γ in Eqn. 1. [13, 14]

$$\Delta \mathrm{G_{def}} \approx \gamma \times \Delta \mathrm{A}, \tag{1}$$

In the original work of Stillinger,[15] only liquid-vapor interfaces were considered, however later work by Ladanyi adapted capillary wave theory to account for the coupling of the two surfaces (the organic and the aqueous) that form the liquid-liquid interface.[16] That work noted that more complete description of the surface Hamiltonian were needed to account for surface curvature effects, for example those induced by surfactants.

Understanding surfactant affects upon surface geometry is in its nascent stages. Given that ΔA is an average over the broad ensemble of topographical geometric characteristics, systems with similar ΔA or γ may have very different topographical characteristics; while ΔG_{def} may be proportional to ΔA, the geometric characteristics that influence interfacial reactivity may exhibit complex nonlinear relationships. For example, sodium(alkyl)benzenesulfonates surfactants exhibit an exponential decrease in interfacial tension with an increase in concentration.[17] Additionally, a longer chain length in these surfactants significantly enhanced the effectiveness in reducing interfacial tension, even at lower concentrations. A systematic understanding of the impact of surfactant adsorption upon surface fluctuations, the geometry and topography is essential for understanding numerous chemical and biological processes that occur at interfaces.[18] While significant efforts have been made toward understanding the geometrical properties of surfaces, including properties like curvature and interfacial width, and integrating these factors into the capillary wave theory, very little work has been done on surfactant affects.[19–23] Toward this end, we examine the effects of surfactant surface enrichment or variations in chain lengths on surface fluctuations of the Willard-Chandler representation[24] of the water/air surface. We compare and contrast different geometric measures, such as surface curvature and orientation, to determine their sensitivity to surfactant perturbations and their relation to ΔA. While some systems are in good agreements with capillary wave theory, changing solubilites of surfactants to induce solute con-

centration gradients on the aqueous side of the phase boundary leads to large non-linear changes in surface geometries.

System Configurations. Initial system configurations were generated using the Packmol package,[25] and consisted of a water phase whose air interface contains adsorbed surfactant. Each rectangular box had dimensions of 60 × 60 × 180 Å in the x, y, and z directions, respectively. The system consisted of two water/air surfaces as shown in Figure 1. The primary surfactant considered is tributyl phosphate, TBP, whose concentration was increased from 0 (pure water/air) to 240 TBP by increments of 24 TBP. The total number of H_2O was 7205. To understand the effect of the hydrophobic chain length on the surface curvature, we performed additional simulations with trimethylphosphate (TMP), triethylphosphate (TEP), and tripropylphosphate (TPP), where 96 surfactant molecules were added randomly to the two water/air surfaces (48 per interface).

Molecular Dynamics Simulations. All-atom molecular dynamics simulations were performed using the GROMACS software package.[26] Molecular motions were integrated with the Leapfrog motion integrator and a 2 fs timestep at 298 K. Each system was first energy-minimized using the steepest descent algorithm for 50,000 timesteps, followed by a 40 ns simulation in the NVT ensemble, where the last 20 ns of data were used for analyses. The system temperature was maintained constant using the Nose-Hoover thermostat with a 0.1 ps temperature coupling time.[27] Long-range interactions were treated using the particle mesh Ewald summation (PME), and short-range non-bonded interactions were calculated with a cutoff of 16 Å. Hydrogen-containing bonds were constrained using the LINCS algorithm.[28] Water was modeled using the TIP3P model.[29] The GAFF parameters optimized by Ye et al. were used for TBP.[30] The remaining alkyl-phosphate molecules were modeled using the standard General Amber Force Field (GAFF) force fields without additional optimization.[31] Lennard-Jones cross terms were computed using the Lorentz-Berthelot combination rules.

Definition of the Instantaneous Surface. The Willard and Chandler [24, 32] (WC) surface creates a continuous representation of the discrete instantaneous water surface configurations by implementing normalized Gaussian density fields at the molecular position of instantaneous water (O atoms), $\mathbf{r}$:

$$\phi(\mathbf{r},t) = (2\pi\xi^2)^{\frac{-d}{2}}\, exp\left(\frac{-r^2}{2\xi^2}\right) \tag{2}$$

Here, ξ represents the coarse grain length, and d is the dimension of the box. For the instantaneous density of the ith particle in time t

$$\rho(r,t) = \sum_i \delta(r - r_i(t)) \tag{3}$$

and the coarse-grained density field is obtained as

$$\rho'(r,t) = \phi(\mathbf{r};\xi). \tag{4}$$

The density field $\rho'(r,t)$ is interpolated on a spatial grid that covers the simulation cell. The density field configuration of the slab coexisting with the air phase represents the instantaneous air/water surface, as shown in Figure 1. The Marching-cube algorithm (MCA),[33] as implemented in the Pytim package,[34] is used to obtain the instantaneous surface. MCA scans the density within each grid and generates vertices and triangulated faces based on the presence of density within the cubic grids. We adopt the suggested coarse grain length criterion of 2.5 Å and 90% bulk density to obtain the instantaneous surface of the water. Ensemble average values of the interfacial area are obtained by averaging the individual areas of the instantaneous interfaces (comprised of the triangulated faces) for each system. The time-average change in the interface area, ΔA, is computed as:

$$\Delta A = \frac{1}{t}\sum_t A(\rho^{'}(r,t)) - A, \tag{5}$$

where $A(\rho^{'}(r,t))$ is the instantaneous surface area, and A is the flat surface area, i.e., the product of x and y box lengths (xy Å^2). To calculate the free energy of deformation (Eqn. 1), the surface tension is obtained using the pressure tensor method as an integral over the z dimension with a box length L_z.[35]

Surface Fluctuations of the Instantaneous Surface. The interfacial width (d) is a measure of the surface fluctuations along the z axis and is obtained by fitting the distribution of water density along the z-axis using the Senapati and Berkowitz function[36]:

$$\rho_w(z) = \frac{1}{2}\rho_w - \frac{1}{2}\rho_w\, \mathrm{erf}\left(\frac{z - z_{0,w}}{\sqrt{2}\,d}\right) \tag{6}$$

Here, erf is the error function, ρ_w is the bulk water density, and $z_{0,w}$ is the average position of the interface.

Similar to d, surface roughness (S_r) measures the surface fluctuations along the z axis but in the discretized representation via the z coordinates of the vertices ($h_i(z)$) within the triangulated mesh:

$$S_r = \sqrt{\frac{1}{N}\sum_i d_i^2}. \tag{7}$$

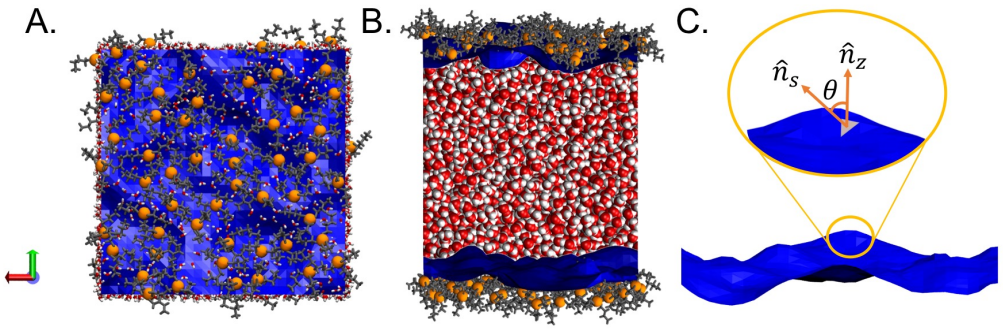

FIG. 1: Schematic of (A) vertical and (B) horizontal views of the simulated water/TBP/air system (TBP = tributyl phosphate). The instantaneous Willard-Chandler (WC) surface is shown in blue. (C) Illustration of the surface orientation angle obtained from the triangulated WC surface.

Here, $d_i = h_z(i) - \langle h_z \rangle$ and N represents the total number of vertices in the surface mesh.[37] Note that S_r is averaged over the two water/air surfaces in the system.

An autocorrelation function that measures time dependent deviations of the average height h and surface roughness S_r from its mean was employed using the equation

$$C_h(t) = \langle \delta h(0)\, \delta h(t) \rangle \tag{8}$$

where $\delta h(t) = h(t) - \langle h(t) \rangle$.[38]

Measures of Surface Geometry. Surface curvature characterizes the degree to which the instantaneous surface deviates from a planar analogue. In 2-dimensions, the curvature is the inverse of the radius of curvature, $\kappa_2 = 1/r$. Extending this to three dimensions, the curvature at each point is defined by two principal curvatures, κ_1 and κ_2. These are employed to define the mean and Gaussian curvature. The mean curvature, denoted as $\kappa_m = (\kappa_1 + \kappa_2)/2$, measures the average surface bending. A value of $\kappa_m < 0$ or > 0 represents concave and convex surfaces, respectively, while $\kappa_m = 0$ represents a flat average surface [39–44]. The Gaussian curvature is the product of the two principal curvatures (κ_1 and κ_2) ($\kappa_G = \kappa_1.\kappa_2$) and reflects the surface topography. For instance, in a torus, the convex region has a positive κ_G and the inner concave region has a negative κ_G. We further defined the shape descriptor, curvedness κ_C^2, at each surface point q_i, using the two principal curvatures κ_1 and κ_2 as

$$\kappa_C^2(q_i) = \kappa_1^2(q_i) + \kappa_2^2(q_i), \tag{9}$$

where the average surface curvedness for the instantaneous surface is

$$\kappa_C^2 = \frac{1}{N} \sum_{i=1}^{N} \kappa_C^2(q_i), \tag{10}$$

which has N as the total number of vertices. Importantly, curvedness describes the total magnitude of surface curvedness irrespective of positive or negative principle curvature. Thus, higher values of κ_C^2 in the case of a liquid/liquid surface indicate higher surface fluctuations.[45, 46]

Surface orientation is an additional measure of the geometry and is calculated by taking the dot product of the surface normal $\hat{n}_s$ (at each surface triangle) with a unit vector $\hat{n}_z$ along the z-axis. The ensemble average orientation is obtained by taking the mean of all surface normal orientations as

$$\langle \theta_s \rangle = \langle \hat{n}_s.\hat{n}_z \rangle_i. \tag{11}$$

Here, i represents the surface mesh-triangles. The ensemble-average orientation is further time-averaged over the entire trajectory.

Concentration Dependence of Surface Properties. Although comprehensive studies have been conducted on the subject of aqueous/air interfaces, a majority of these investigations have focused predominantly on macroscopic surface characteristics, including, but not limited to, surface tension and width as a function of different surfactant characteristics and concentration.[47–51] Extensive studies have further examined the orientation of polar solvents at the liquid/air interface through use of surface sensitive spectroscopies, as well as solute concentration gradients and organization at the surface.[52–55] Yet, connecting the surfactant adsorption to the geometry of the interface and its fluctuations is relatively unexplored. The geometric properties of the surface is of growing importance because local surface organization creates microenvironments for reactivity.[56–59] We begin this study by examining geometric measures and their fluctuations of the instantaneous surface as a function of surfactant concentration, specifically TBP.

n_{TBP}	Surface coverage (n/Å^2)	d (Å)	γ (mN/m)	ΔA (Å^2)	ΔG_{def} (kJ/mol)
0	0	1.82	47.80 ± 0.14	52.37	25.03
48	0.0064	2.21	46.91 ± 0.18	258.61	121.31
96	0.0126	2.41	44.30 ± 0.25	423.88	187.78
144	0.0184	3.62	39.57 ± 0.44	632.06	250.11
240	0.0291	4.68	36.03 ± 0.61	1059.86	381.87

TABLE I: Surface coverage of TBP, interfacial width d, surface tension γ, the change in surface area ΔA and free energy of surface deformation ΔG_{def} as a function of TBP coverage at the water/air surface.

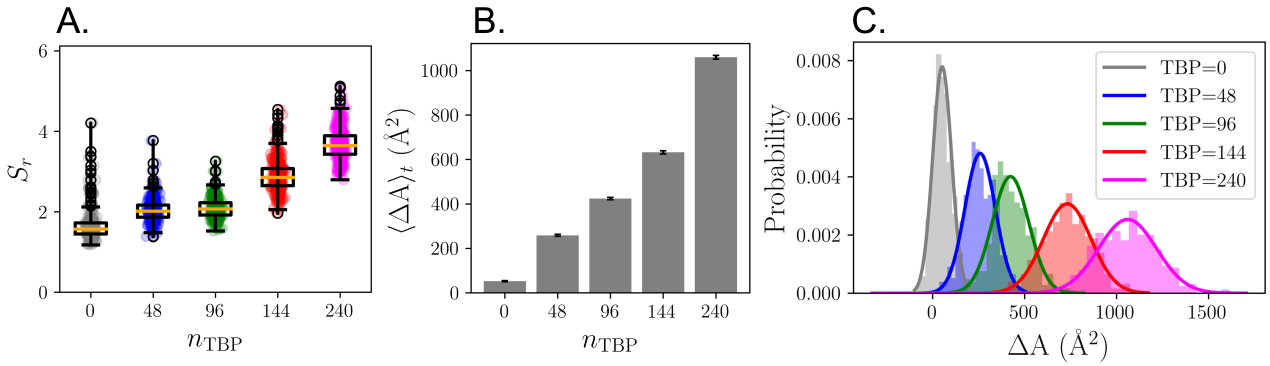

FIG. 2: (A.) Surface roughness (S_r) as a function of n_{TBP} at water/air surface. The orange line in the boxplot signifies the median value, while the boundaries denote the 25th and 75th percentiles of the dataset. The individual circles represent the outliers. (B.) Mean instantaneous water/air surface area and the respective standard deviations (plotted as error bars and obtained using the equation $\sigma/\sqrt{n}$, where σ is obtained from fitted Gaussian distribution functions).(C.) Distributions of ΔA for varying numbers of adsorbed TBP. An illustration of the gaussian fitting of ΔA is provided in the Figure S2.

As observed in Table I, the surface tension γ decreases from 47.80 ± 0.14 to 36.03 ± 0.61 mN/m as n_{TBP} increases from 0 to 240. Concurrently, there is an increase in interfacial width d (Table I) and surface roughness S_r (Figure 2A). The increase in S_r and d indicate enhancement of the surface fluctuation perpendicular to the interfacial plane (the z-axis) with an increase of TBP surface coverage. Although the surface tension decreases by nearly 25%, the pronounced change in ΔA leads to a significant increase in the free energy of surface deformation with increasing TBP, from 25.03 kJ/mol in the pure air interface to 381.87 kJ/mol at $n_{TBP} = 240$. As shown in Figure 2B, the average change to surface area increases linearly with TBP surface coverage, however, this belies a significant change to the distribution of surface areas observed within the simulation trajectory. The ensemble distribution systematically becomes more broad (Figure 2C), the full width of half maximum (FWHM) of the fitted Gaussians increased ∼3× from the pure air interface to the highest TBP surface coverage, indicating large variations in the spatial fluctuations of the instantaneous surface.

Increases to spatial capillary wave fluctuations may occur homogeneously or inhomogeneously depending upon the competition of surfactant-surfactant vs. surfactant-surface interactions. For example, there may exist areas of high curvature and areas of low curvature if the TBP does not form a homogeneous monolayer. In liquid/liquid systems, it is well-known that TBP self-asssembles at the interface to form dimers that can further assemble into larger macrostructures responsible for solute transport.[7] The structural origins behind the the general changes to the surface structure that are defined by γ, d, S_r, and ΔA are now analyzed by studying the average and ensemble distributions of different geometric measures.

We first examine the average surface orientation, which increases linearly ($R^2 = 0.97$) with the addition of TBP at the water/air surface (Figure S3). Study of the surface orientation θ_s° probability distributions (Figure 3A) shows that the peak maximum systematically increases with little change to the width of the distribution until a concentration of 240 TBP at which point there is a significant broadening and the formation of a shoulder in the distribution. Complementing this information is the measure curvedness κ_C^2(Eqn.10)[45], which describes

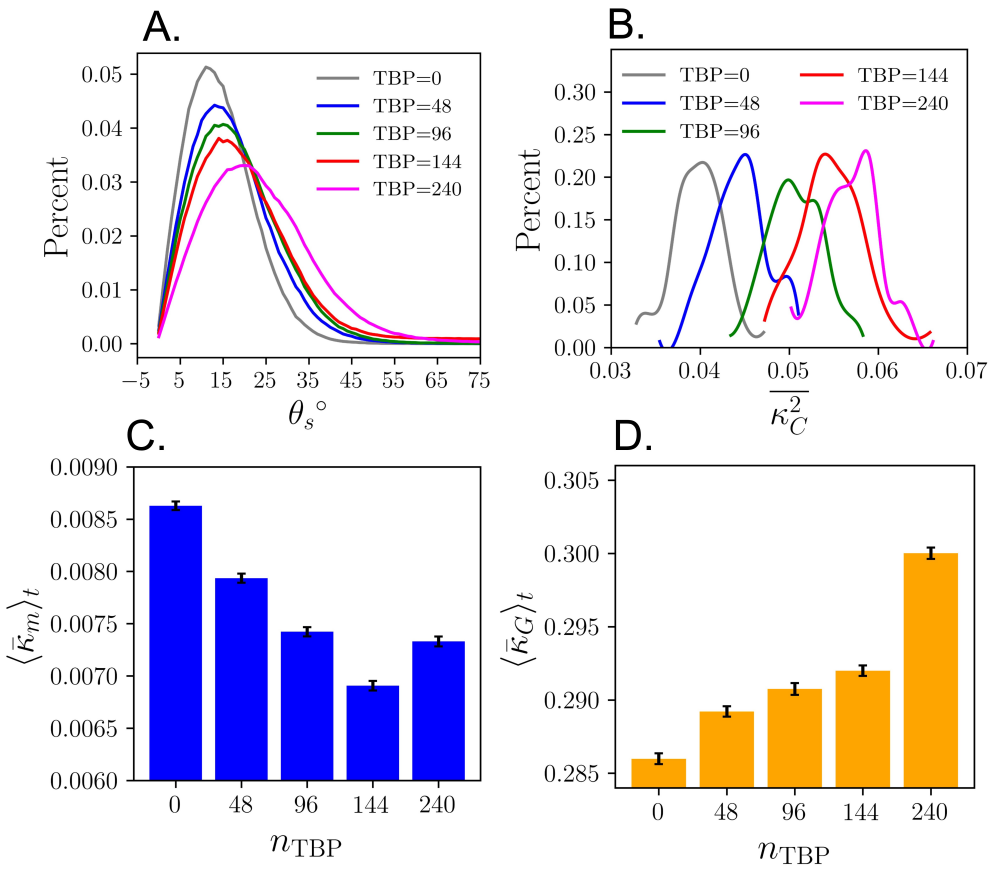

FIG. 3: (A.) The distributions of the surface normals orientation with increased TBP at water/air surface. (B.) The distribution of surface curvedness as a function of TBP adsorbed at the water/air surface. (C.) Mean curvature and (D.) Gaussian curvature as a function of the number of adsorbed TBP at water/air interface. The bar indicates the average calculated at each individual point on the surface, while the bracket signifies the average taken across all snapshots.

the true curvature of the surface, irrespective of its sign corresponding to surface concavity or convexity. Higher values of curvedness represent more sharp (less broad) capillary wave features. The distributions of ^2_C are presented in Figure 3C. Addition of surfactant adds features to a nominal gaussian distribution observed at n_{TBP} as the concentration is increased. Interestingly, a comparison of the mean ($_m$) and Gaussian ($_G$) curvatures reveals distinctly different behavior between $n_{TBP} = 144$ and 240. A linear decrease in κ_m is observed from the pure water/air interface until $n_{TBP} = 144$ is reached. This indicates that there is increasing cancellation of the convex and concave portion of the capillary wave behavior. At $n_{TBP} > 144$ an increase in κ_m is observed. At the same time, the average $_G$ increases in a close to the linear manner up to $n_{TBP} = 144$, then a large jump occurs at $n_{TBP} = 240$. At this highest concentration, a significant shoulder is observed on the higher end of the curvedness distribution is observed (Figure 3). The combination of these data indicates that as the TBP concentration is systematically increased, the TBP enhances surface curvature while the average bending decreases (the convexity and concavity cancel) - we label this behavior a homogenous increase to the surface fluctuations. Above $n_{TBP} = 144$, there is a significant change in the surface geometry, this is consistent with TBP self assembly where hydrogen bonding of H_2O between multiple TBP molecules severely disrupts intermolecular water hydrogen bonding to enhance topographical heterogeneity.

To understand the impact of surfactant adsorption on the dynamics of surface fluctuations, time correlation functions of h and κ_C^2 are computed using Eqn. 8. It is observed that both h and κ_C^2 relaxes to 10% of its initial value within 0.01 ns in the pure liquid interface compared to 1 ns in the TBP = 240 system (Figure S5). The increase in TBP concentration delays the relaxation of the surface fluctuations, showing an inverse correlation between surface tension and relaxation (i.e., slow relaxation with an increase in surface tension or surface heterogeneity). At low TBP surface coverages the correlation time

is nearly identical for curvedness and height as would be expected from capillary waves, yet at the highest TBP concentrations, there are variations in the long-time correlations indicating changes to the timescales of the curvature evolution vs. height evolution. One might expect that in concentration regimes where TBP-TBP interactions dominate and become localized (as in self-assembly) that such variations may occur.

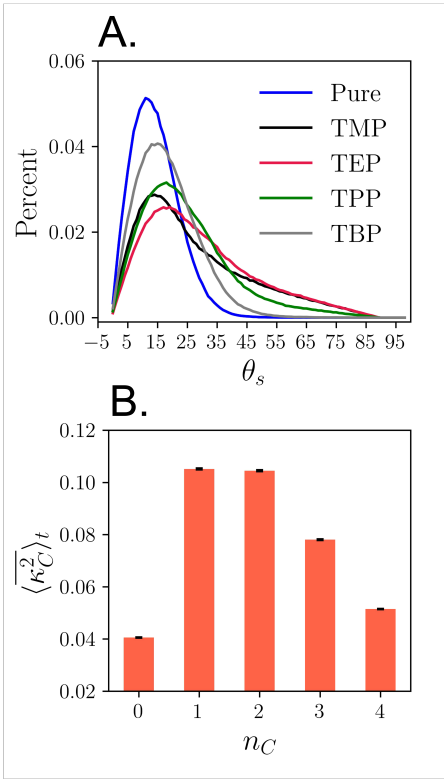

FIG. 4: (A) The distributions of the surface normals orientation for different trialkyl phosphates adsorbed at water/air surface. (B) Mean surface curvedness of the water/air surface with adsorbed trialkyl phosphates of different chain lengths.

Role of Surfactant Tail Length. The length of the associated alkyl chain on the phosphate head group dramatically changes the aqueous solubilities of TBP (∼0.28-0.4 g/L), TPP (6.951 g/L) and TEP (15.9 g/L).[60–62] This solubility variation, in turn, affects the surface concentration of these surfactants while having a constant total concentration in the system. Consequently, the relationship between alkyl chain length and surface fluctuations exhibits greater complexity than previously understood. As shown in Table II, lower solubility surfactants predominantly accumulate at the water/air interface relative to those with higher solubility or shorter alkyl chains. Despite the surface tension (γ) remaining within a range of 30-50 mN/m, we observed a notable elongation in the interfacial width (d) with increasing alkyl chain length to n=3 (Table II), which decreased from TPP to TBP. These behaviors are closely related to the intermolecular interactions between the phosphate (O=P) headgroup and water molecules, and their influence on the hydrogen-bonding network of the water at the interface. The highly water-soluble TEP significantly perturbs the hydrogen-bonding structure of the interfacial water, while exhibiting the highest degree of solvating around the O=P group (Table S2).

Interestingly, despite the TEP exhibiting lower surface coverage, its extensive interaction with water significantly influences the change in surface area (ΔA) more than TBP, which possessed greater surface concentration. As illustrated in Table II, the addition of TMP to the pure water/air surface increased the average surface area to $\sim$ 4000 Å^2 (refer to C_1-pure), which further increased by $\sim$ 500 Å^2 with the addition of a -CH_3 group to TMP. Subsequent increases in surfactant tail length led to a decrease in surface area compared to TEP. In general, the area followed the trend TEP > TMP > TPP > TBP > Pure. The ensemble-averaged surface orientation exhibited similar trends. The surface orientation distributions and curvedness as a function of the TAP alkyl tail length are plotted in Figure 4. The orientation trend followed a Gaussian distribution model with a sigma value of 1.85 $\pm$ 0.19 (Figure S6). The surface orientation distribution reveals the elongation of the distribution toward higher θ values, showing a skewed Gaussian distribution), which primarily reflects the enhanced efficiency of TEP in forming and amplifying the capillary wave surface fluctuations relative to other alkyl phosphates. A similar skewed Gaussian distribution trend is observed for surface curvedness (Figure 4 B and S7).

Relationships Between Surface Geometry and Macroscopic Properties

We next compare surface geometric descriptors, namely curvature and mean surface orientation angle, against macroscopic surface properties, such as surface tension and the free energy of surface deformation. A direct linear relationship is observed between these geometric descriptors and macroscopic properties (Figure 5). The correlations show an escalation in surface heterogeneity which reduces γ while concurrently augmenting surface curvature and mean surface orientation angle. Similarly, an increase in surfactant concentration at the water/air interface creates a surface that is more susceptible to deformation, thereby inducing an elevation in both curvature and surface orientation. These correlations propose that surface geometry descriptors directly correspond with macroscopic surface properties and can be contrasted with empirically detected observables, warranting their incorporation into analytic model development, similar to what was demonstrated by Ladanyi

Chain length n_C	Surface coverage (n/Å^2)	d Å	γ(mN/m)	ΔA (Å^2)	Δ G$_{\text{def}}$(kJ/mol)
1 (TMP)	0.0032	2.01	45.77 ± 0.48	3851.23	1762.70
2 (TEP)	0.0054	2.45	41.45 ± 0.21	4501.94	1866.05
3 (TPP)	0.0098	2.87	34.38 ± 0.11	1876.04	644.98
4 (TBP)	0.0126	2.41	44.30 ± 0.25	423.87	187.78

TABLE II: Surface coverage of alkyl phosphates with different C-chain lengths (TMP = trimethyl phosphate, TEP = triethyl phosphate, TPP = tripropyl phosphate, TBP = tributyl phosphate). Interfacial width d, surface tension γ, the change in surface area Δ A and free energy of surface deformation ΔG_{def} as a function of surface coverage at the water/air surface are provided.

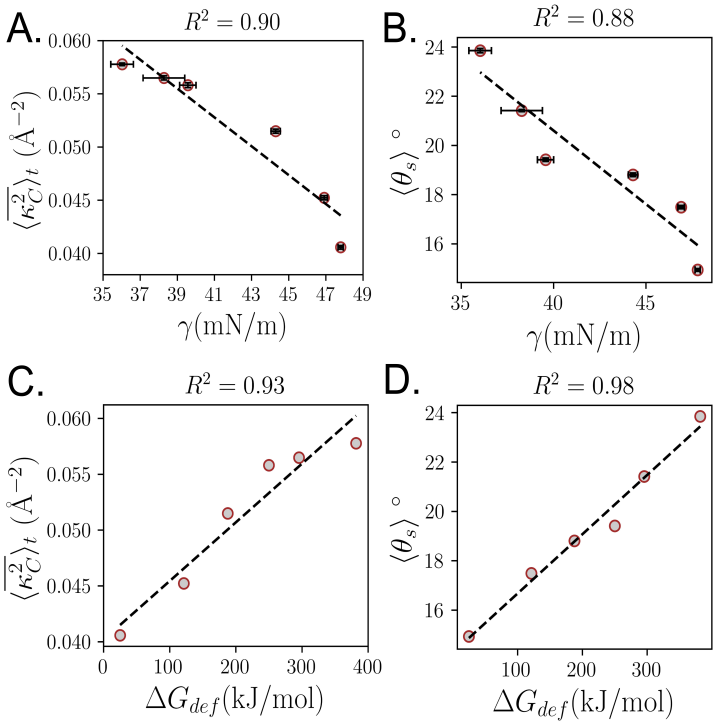

FIG. 5: (A) The time-averaged surface curvedness (B) average surface orientation angle as a function of surface tension, fitted to a linear regression model. (C) Surface curvedness, (D) average surface orientation angle as a function of the free energy of deformation due to surfactant adsorption water/air surface.

et al. for the surface fluctuations at pure liquid/liquid interfaces.[19]

In summary, this work explores the impact of surfactant upon the geometric properties of the liquid/vapor interface. In the case of concentration dependent TBP, expected changes to the surface tension and deformation are observed in agreement with capillary wave theory. Our results indicate that an increased surfactant surface concentration leads to augmented surface area and curvature. Higher curvature values correspond to more pronounced capillary wave features, characterized by sharper, less broad waves. Our data suggest a systematic relationship whereby increasing TBP concentration enhances surface curvature, while simultaneously reducing the average bending due to a balancing of convexity and concavity. This phenomenon caused a homogeneous increase in surface fluctuations, which aligns with the self-assembly behavior of TBP. Yet the relaxation timescales of the surface show an unanticipated inverse relationship. As the surface deformation increases, the relaxation timescale is increased - taking a longer time to relax. in the case of surfactants that systematically increase their water solubility (by decreasing the length of the alkyl tails attached to the phosphate head group), increasing the solubility of the surfactant decreases the surface concentration but unexpectedly increases the mag-

nitude of the surface fluctuations.

The authors acknowledge the Department of Energy, Basic Energy Sciences Separations program (DE-SC0001815) for funding.

[1] O. Bjorneholm, M. H. Hansen, A. Hodgson, L.-M. Liu, D. T. Limmer, A. Michaelides, P. Pedevilla, J. Rossmeisl, H. Shen, G. Tocci, et al., Chemical reviews **116**, 7698 (2016).

[2] R. Kusaka, S. Nihonyanagi, and T. Tahara, Nature Chemistry **13**, 306 (2021).

[3] B. Ocko, X. Wu, E. Sirota, S. Sinha, and M. Deutsch, Physical review letters **72**, 242 (1994).

[4] A. E. Ismail, G. S. Grest, and M. J. Stevens, The Journal of chemical physics **125** (2006).

[5] D. Schwartz, M. Schlossman, E. Kawamoto, G. Kellogg, P. S. Pershan, and B. Ocko, Physical Review A **41**, 5687 (1990).

[6] T. Zhou, A. McCue, Y. Ghadar, I. Bakó, and A. E. Clark, The Journal of Physical Chemistry B **121**, 9052 (2017), pMID: 28871781, https://doi.org/10.1021/acs.jpcb.7b07406, URL `https://doi.org/10.1021/acs.jpcb.7b07406`.

[7] M. J. Servis and A. E. Clark, Physical Chemistry Chemical Physics **21**, 2866 (2019).

[8] N. Kumar and A. E. Clark, Chemical Science **12**, 13930 (2021).

[9] P. Morgado, O. Lobanova, E. A. Müller, G. Jackson, M. Almeida, and E. J. Filipe, Molecular physics **114**, 2597 (2016).

[10] G. M. Silva, P. Morgado, P. Lourenço, M. Goldmann, and E. J. Filipe, Proceedings of the National Academy of Sciences **116**, 14868 (2019).

[11] M. L. Schlossman and A. M. Tikhonov, Annu. Rev. Phys. Chem. **59**, 153 (2008).

[12] A. Pohorille and I. Benjamin, The Journal of Physical Chemistry **97**, 2664 (1993).

[13] H. W. Huang, Biophysical journal **50**, 1061 (1986).

[14] V. Venkateshwaran, S. Vembanur, and S. Garde, Proceedings of the National Academy of Sciences **111**, 8729 (2014).

[15] F. P. Buff, R. A. Lovett, and F. H. Stillinger, Phys. Rev. Lett. **15**, 621 (1965).

[16] J. Chowdhary and B. M. Ladanyi, Phys. Rev. E **77**, 031609 (2008).

[17] B. Smit, A. G. Schlijper, L. A. M. Rupert, and N. M. Van Os, The Journal of Physical Chemistry **94**, 6933 (1990).

[18] M. Lbadaoui-Darvas, A. Idrissi, and P. Jedlovszky, The Journal of Physical Chemistry B **126**, 751 (2021).

[19] J. Chowdhary and B. M. Ladanyi, Physical Review E **77**, 031609 (2008).

[20] C. Fradin, A. Braslau, D. Luzet, D. Smilgies, M. Alba, N. Boudet, K. Mecke, and J. Daillant, Nature **403**, 871 (2000).

[21] J. Stecki, The Journal of chemical physics **109**, 5002 (1998).

[22] L. G. MacDowell, Phys. Rev. E **96**, 022801 (2017), URL `https://link.aps.org/doi/10.1103/PhysRevE.96.022801`.

[23] J. Hernández-Muñoz, P. Tarazona, and E. Chacón, The Journal of Chemical Physics **157**, 154703 (2022), ISSN 0021-9606.

[24] A. P. Willard and D. Chandler, The Journal of Physical Chemistry B **114**, 1954 (2010).

[25] L. Martínez, R. Andrade, E. G. Birgin, and J. M. Martínez, Journal of computational chemistry **30**, 2157 (2009).

[26] M. J. Abraham, T. Murtola, R. Schulz, S. Páll, J. C. Smith, B. Hess, and E. Lindahl, SoftwareX **1**, 19 (2015).

[27] D. J. Evans and B. L. Holian, The Journal of chemical physics **83**, 4069 (1985).

[28] B. Hess, H. Bekker, H. J. Berendsen, and J. G. Fraaije, Journal of computational chemistry **18**, 1463 (1997).

[29] E. Neria, S. Fischer, and M. Karplus, The Journal of chemical physics **105**, 1902 (1996).

[30] X. Ye, S. Cui, V. F. de Almeida, and B. Khomami, The Journal of Physical Chemistry B **117**, 14835 (2013).

[31] J. Wang, R. M. Wolf, J. W. Caldwell, P. A. Kollman, and D. A. Case, Journal of computational chemistry **25**, 1157 (2004).

[32] Z. Liu, T. Stecher, H. Oberhofer, K. Reuter, and C. Scheurer, Molecular Physics **116**, 3409 (2018).

[33] W. E. Lorensen and H. E. Cline, ACM siggraph computer graphics **21**, 163 (1987).

[34] M. Sega, G. Hantal, B. Fábián, and P. Jedlovszky, *Pytim: A python package for the interfacial analysis of molecular simulations* (2018).

[35] J. Alejandre, D. J. Tildesley, and G. A. Chapela, The Journal of chemical physics **102**, 4574 (1995).

[36] S. Senapati and M. L. Berkowitz, Physical review letters **87**, 176101 (2001).

[37] B. Suhr, W. A. Skipper, R. Lewis, and K. Six, Scientific Reports **10**, 1 (2020).

[38] J. Mittal and G. Hummer, Proceedings of the National Academy of Sciences **105**, 20130 (2008).

[39] Y. A. Omar, A. Sahu, R. A. Sauer, and K. K. Mandadapu, Biophysical journal **119**, 1065 (2020).

[40] H. Alimohamadi and P. Rangamani, Biomolecules **8**, 120 (2018).

[41] N. A. Garcia, A. D. Pezzutti, R. A. Register, D. A. Vega, and L. R. Gómez, Soft Matter **11**, 898 (2015).

[42] M. Hu, J. J. Briguglio, and M. Deserno, Biophysical journal **102**, 1403 (2012).

[43] S. Yesylevskyy and C. Ramseyer, Physical Chemistry Chemical Physics **16**, 17052 (2014).

[44] C. D. Gale, M. Derakhshani-Molayousefi, and N. E. Levinger, The Journal of Physical Chemistry B **126**, 953 (2022).

[45] J. J. Koenderink and A. J. Van Doorn, Image and vision computing **10**, 557 (1992).
[46] S. Z. Li, Computer-Aided Design **27**, 235 (1995).
[47] H. S. Alasiri, A. S. Sultan, and W. G. Chapman, Energy & Fuels **33**, 6678 (2019).
[48] Chemical Physics Letters **373**, 87 (2003), ISSN 0009-2614.
[49] C. Vega and E. de Miguel, The Journal of chemical physics **126** (2007).
[50] M. Peng, T. T. Duignan, C. V. Nguyen, and A. V. Nguyen, Langmuir **37**, 2237 (2021).
[51] H. B. de Aguiar, A. G. de Beer, M. L. Strader, and S. Roke, Journal of the American Chemical Society **132**, 2122 (2010).
[52] S. Nihonyanagi, J. A. Mondal, S. Yamaguchi, and T. Tahara, Annual review of physical chemistry **64**, 579 (2013).
[53] H. C. Allen, D. Gragson, and G. Richmond, The Journal of Physical Chemistry B **103**, 660 (1999).
[54] N. Kumar, M. J. Servis, and A. E. Clark, Solvent Extraction and Ion Exchange **40**, 165 (2022).
[55] B. Doughty, P. Yin, and Y.-Z. Ma, Langmuir **32**, 8116 (2016).
[56] E. Alvarado, Z. Liu, M. J. Servis, B. Krishnamoorthy, and A. E. Clark, Journal of Chemical Theory and Computation **16**, 4579 (2020).
[57] N. Kumar and A. E. Clark, Journal of Chemical Theory and Computation **19**, 3303 (2023).
[58] N. Zarayeneh, N. Kumar, A. Kalyanaraman, and A. E. Clark, Journal of Chemical Theory and Computation **18**, 7043 (2022).
[59] S. W. Devlin, I. Benjamin, and R. J. Saykally, Proceedings of the National Academy of Sciences **119**, e2210857119 (2022).
[60] P. Velavendan, S. Ganesh, N. Pandey, R. Geetha, M. Ahmed, U. Kamachi Mudali, and R. Natarajan, Journal of Radioanalytical and Nuclear Chemistry **295**, 1113 (2013).
[61] C. Higgins, W. Baldwin, and B. Soldano, The Journal of Physical Chemistry **63**, 113 (1959).
[62] W. Apostoluk and W. Robak, SN Applied Sciences **1**, 801 (2019).